

Circulation and melting beneath George VI Ice Shelf, Antarctica

Adrian Jenkins¹ and Stan Jacobs²

¹*British Antarctic Survey, Natural Environment Research Council,
High Cross, Madingley Road, Cambridge, CB3 0ET, U.K.*

²*Lamont-Doherty Earth Observatory of Columbia University,
Route 9W, Palisades, New York, NY 10964, U.S.A.*

Introduction

George VI Ice Shelf, sandwiched between the western coast of Palmer Land and the eastern coast of Alexander Island, is the largest and most studied of the west Antarctic Peninsula ice shelves. It covers an area of approximately 25,000 km² and is underlain by Circumpolar Deep Water (CDW), with temperatures in excess of 1°C, giving rise to rapid basal melting (Bishop and Walton, 1981; Lennon et al., 1982). The maximum ice thickness of about 500 m occurs about 70 km from the southern ice front, where a ridge of thick ice extends across George VI Sound (near 70°W, see Figure 1) effectively dividing the upper water column into northern and southern regions. The northern ice front, which faces Marguerite Bay, appears to be near the geographical limit of ice shelf viability and has undergone a gradual retreat in recent decades (Lucchitta and Rosanova, 1998), a timeframe over which much of the nearby Wordie Ice Shelf disintegrated (Doake and Vaughan, 1991). There is extensive surface melting over the northern parts of the ice shelf and much of the ice column near the northern ice front appears to be temperate (Paren and Cooper, 1986). Conditions in the south, where the ice front faces into Ronne Entrance, are colder and the ice front position appears to be steady. The vast majority of the flow into the ice shelf comes from Palmer Land, but basal melting is sufficient to remove most of this, so that the ice is derived almost exclusively from local accumulation by the time it reaches the ice fronts (Potter et al., 1984). There is some evidence at the margins of the ice shelf to suggest that it may have disappeared completely during the early Holocene before reforming (Sugden and Clapperton, 1981; Bentley et al., 2005).

During the 1980's a programme of research was conducted into the interactions between the ice shelf and the underlying CDW. The main findings were summarised by Potter and Paren (1985). The work was focussed predominantly near the northern ice front, where rifts in the ice shelf allowed easy access for oceanographic instruments lowered into the water column. The circulation proposed was one in which CDW was drawn beneath the ice shelf, where melting drove upwelling and an outflow that was concentrated in the west. Potter et al. (1988) added some more detail to this picture, deriving geostrophic velocities from a temperature and salinity section measured along the northern ice front. They found weak flow ($< 2 \text{ cm s}^{-1}$) over much of the section with a number of inflows, near the eastern margin and the seabed, balancing an intense surface outflow in the west. Potter et al. (1988) also discussed measurements made at the southern ice front, but these were more scattered and the only continuous section included only temperature data.

In March 1994 we obtained oceanographic measurements, including continuous profiles of temperature, salinity and dissolved oxygen as well as discrete point observations of the oxygen isotope ratio and dissolved helium concentration, at both the northern and southern ice fronts of George VI Ice Shelf (Figure 1) from the research icebreaker *Nathaniel B Palmer*. These data represent the most complete, near-contemporaneous sampling of conditions at both ice fronts that has been made to date. Here we discuss the continuous

profile data and show how they can be used to estimate the concentration of meltwater derived from the ice shelf that is present in the water column. We then derive geostrophic velocities across each section from the density data and use the inverse method described by Wunsch (1978) to apply constraints on the overall transports into and out of the sub-ice-shelf cavity. We investigate how well this technique enables us to constrain the net meltwater production rate within the cavity.

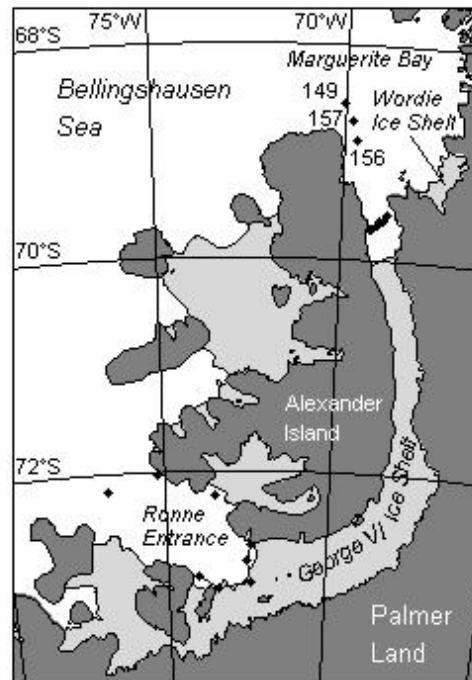


Figure 1: Map of George VI Sound showing the location of CTD stations discussed in the paper. Those comprising the northern and southern ice front sections are connected by lines. In addition there are three far-field stations (numbered in the north) near each section. At the time of the study fast ice occupied the area between the northern section and the ice shelf

Data

The oceanographic sections discussed in this paper were occupied during cruise NBP9402 to the Amundsen and Bellingshausen seas (Giulivi and Jacobs, 1997). Although we focus our attention primarily on the sections obtained near George VI ice fronts, we set those data in their wider context by reference to other oceanographic stations occupied during the same cruise in the eastern Bellingshausen Sea (Figure 1). The stations comprising the southern ice front section were located a few hundred metres seaward of the ice front, while those that form the northern ice front section were occupied while the ship was up against a fast ice edge, about 40 km north of the actual ice front.

The main feature of the water column in this region is the ubiquitous presence of CDW, characterised by relatively high temperature and salinity and low dissolved oxygen, which appears to access all the deeper regions of the continental shelf (Figure 2). Although the CDW found in Marguerite Bay was $\sim 0.1^\circ\text{C}$ warmer than that found in Ronne Entrance, the very warmest temperatures do not appear to reach the northern ice front. The main bathymetric trough in Marguerite Bay originates from George VI Sound, but near 69°S it is at least partially blocked by a ridge of higher ground extending north-east from the coast of

Alexander Island (O’Cofaigh et al., 2005). There appears to be only one narrow gap where the seabed dips to around 1000 m for a few kilometres, and this may be insufficient to allow a significant southward flow of the deepest CDW from the north.

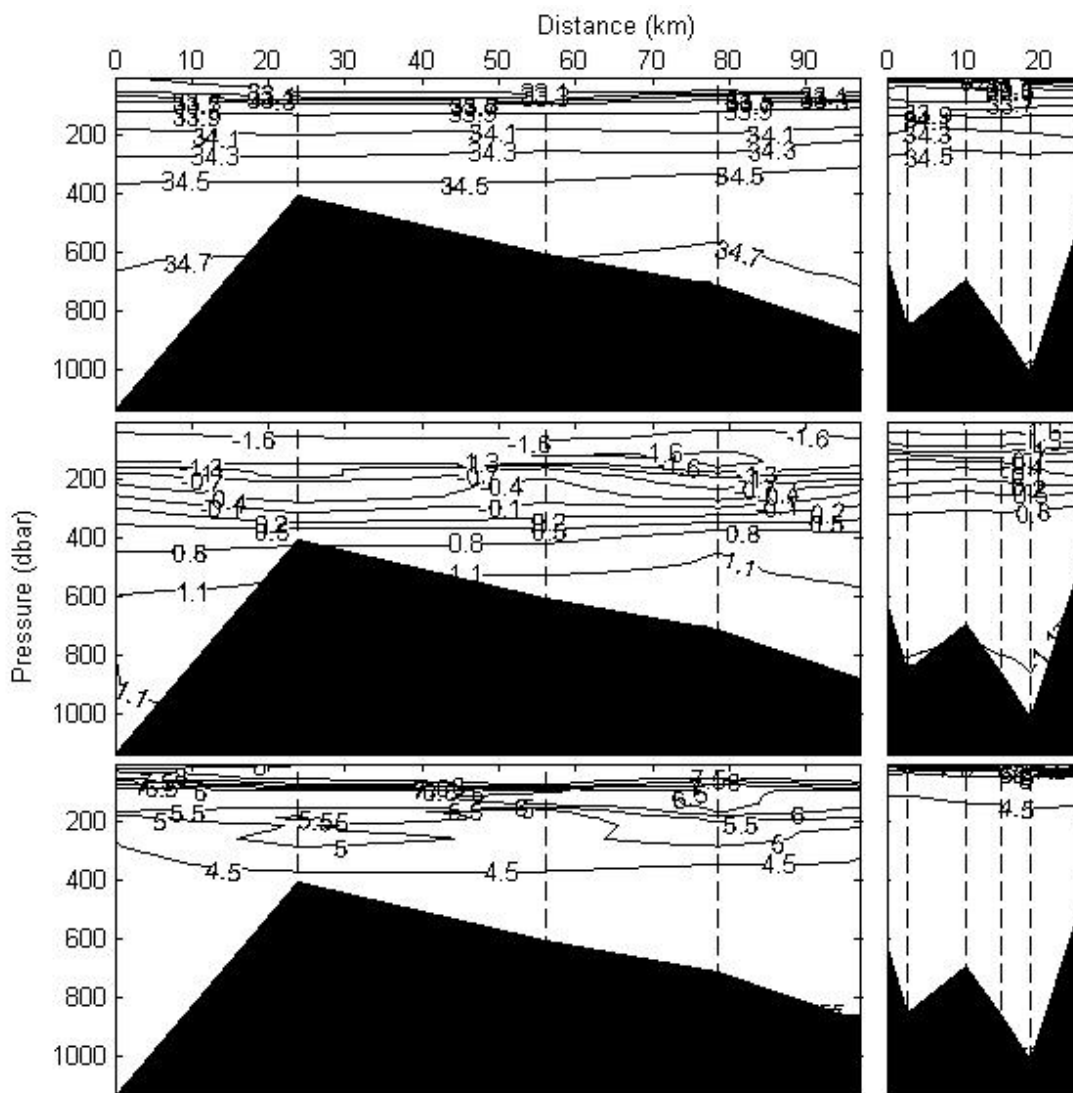


Figure 2: Salinity (top), potential temperature ($^{\circ}\text{C}$, middle) and dissolved oxygen (ml l^{-1} , bottom) recorded at the southern (left) and northern (right) ice fronts. The sections start and end at a CTD station and intermediate stations are indicated by the vertical dashed lines. Both sections are drawn looking out from beneath the ice shelf.

Further evidence for this is provided by the potential temperature/salinity correlations of the data (Figure 3). The far-field stations on the outer continental shelf and beyond the shelf break (not plotted here) show the usual trends from CDW core characteristics ($\theta > 1^{\circ}\text{C}$, $S \approx 34.7$) to remnant Winter Water (WW, $\theta \approx -1.7^{\circ}\text{C}$, $S \approx 34$), and from WW to more variable, warmer and fresher, surface waters. There is a slight cooling of the CDW with progress on-shelf, more pronounced in the south, but other than that the water column changes little until it feels the influence of the ice shelves. At the southern ice front the impact of meltwater is manifested counter-intuitively in the warm, salty intrusions that interrupt the θ/S trend in the main CDW/WW thermocline (Figure 3). The warm/salty extremes of these intrusions have the characteristics of glacier ice melting into the CDW

found at the southern ice front, suggesting that they were formed by melt-driven upwelling of CDW beneath the ice shelf. Potter et al. (1988) found similar melt-driven intrusions at the southern ice front, while the origins of analogous features in the Amundsen Sea were discussed in more detail by Hellmer et al. (1998) and Jenkins (1999). At the northern ice front the CDW/WW thermocline is entirely absent and the whole water column below the shallow surface layer has the characteristics of ice melting into CDW, as noted before by Potter and Paren (1985) and Potter et al. (1988). Close inspection of the CDW endpoint at the northern ice front (Figure 3, inset) shows that it clearly has the properties of that found at the southern ice front. Only the three far-field stations near 69°S show northern CDW characteristics in the lower parts of the water column. The station immediately south of the ridge (number 156, Figure 1) has a mid-depth intrusion of northern CDW, shown even more clearly in the temperature profiles of Figure 4. These are strongly suggestive of northern CDW spilling over and around seabed topography in small enough quantities that the whole of George VI Sound is dominated by CDW flowing in from the south.

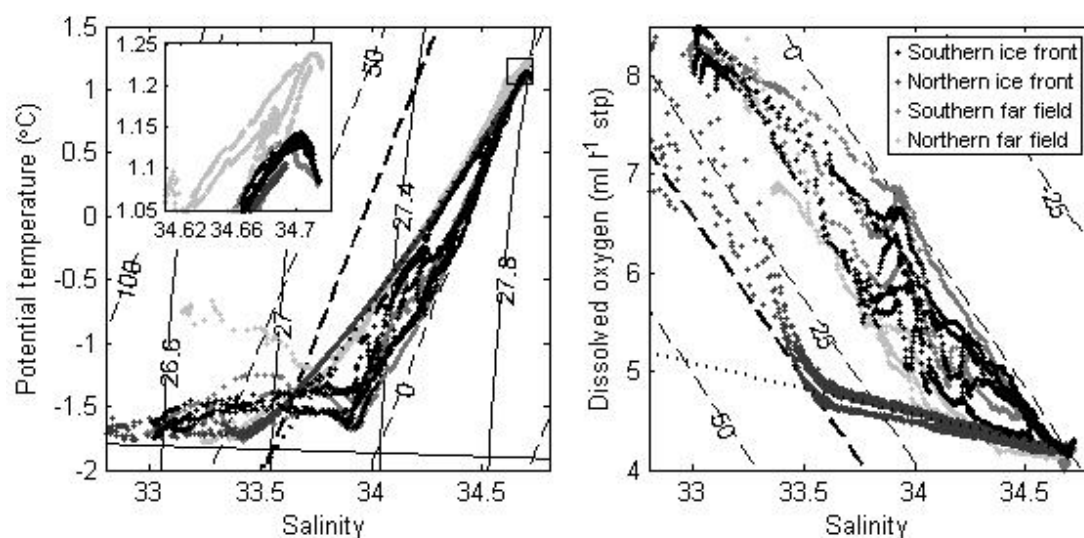


Figure 3: θ/S (left) and O_2/S (right) data obtained at the stations marked in Figure 1. From darkest to lightest the points indicate the southern ice front section, the northern ice front section, the southern far-field stations and the northern far-field stations. The inset panel on the left shows the small box around CDW values enlarged. Isopycnals are plotted on the θ/S diagram. The dashed lines on both diagrams are contours of meltwater fraction (per mille), while the bold dashed line indicates the theoretical upper bound on the melt fraction. The bold dotted lines in each diagram indicate the CDW/meltwater mixing line.

The inflowing CDW carries with it a low dissolved oxygen signature that acts as a valuable tracer (Figure 2). When ice melts from the base of the ice shelf, the oxygen contained within the air bubbles trapped in the ice goes into solution. However, the dissolved oxygen levels that result from this process are significantly lower than those obtained by equilibration with the atmosphere. Thus the presence of upwelled CDW in the water column to the north of the northern ice front is clearly indicated by the anomalously low oxygen levels, even near the surface (Figure 2). On a plot of dissolved oxygen versus salinity (Figure 3), the northern ice front stations are immediately obvious. At any particular salinity they have much lower oxygen concentrations than the ambient water column, which is a mixture of CDW and WW. The latter water mass has acquired its characteristics by interaction with the atmosphere, albeit through a variable sea ice cover, so its dissolved oxygen concentration is generally near saturation. The southern ice front profiles again show the ambient O_2/S

trend, interrupted by oxygen poor intrusions that are mixtures of CDW and meltwater. There is, however, too much variability in the dissolved oxygen data to distinguish clearly between northern and southern CDW.

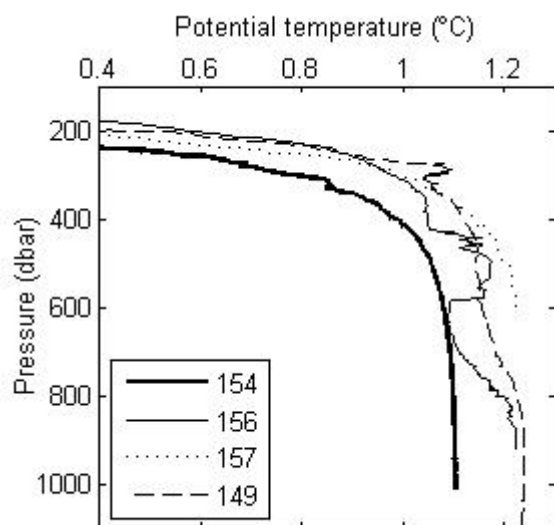


Figure 4: Potential temperature measured between 200 and 1000 dbar at the northern ice front (station 154) and the three far-field stations in the north (see Figure 1 for locations). Stations 156 and 149 lie to the south and north, respectively, of a shallower bank, over which station 157 is positioned.

Meltwater concentrations

The first step in our analysis of the data is to quantify the concentration of meltwater in the water column. At the northern ice front this is a comparatively straightforward task, since the water column is for the most part a simple two-component mixture of CDW and meltwater. We could therefore write a simple conservation equation for any tracer, χ , which could be potential temperature, salinity or dissolved oxygen:

$$\chi_{mix} = (1 - \varphi)\chi_{CDW} + \varphi\chi_{melt} \quad (1),$$

from which the meltwater fraction, φ , could be calculated:

$$\varphi = \frac{\chi_{mix} - \chi_{CDW}}{\chi_{melt} - \chi_{CDW}} \quad (2).$$

However, at the southern ice front the situation is more complex in that WW, with varying properties, is present in significant quantities, and mixes with CDW to form the waters of the main pycnocline. Hence we cannot treat the entire water column as if it were a simple two-component mixture of CDW and meltwater. Since we have measurements of more than one tracer we could write a set of two equations, analogous to (1), for the unknown fractions of meltwater and WW in the three-component mix. An alternative, but equivalent, approach is that adopted by Jenkins (1999). We define a composite of two tracers:

$$\psi^{1,2} = (\chi^2 - \chi_{CDW}^2) - (\chi^1 - \chi_{CDW}^1) \left(\frac{\chi_{WW}^2 - \chi_{CDW}^2}{\chi_{WW}^1 - \chi_{CDW}^1} \right) \quad (3),$$

which has a value of zero for any two-component mixture of CDW and WW. We can then calculate the meltwater fraction directly using the composite tracer in equation (2), which now takes the form:

$$\phi = \frac{\psi_{mix}^{2,1}}{\psi_{melt}^{2,1}} \quad (4).$$

This approach makes it explicit how our choice of a single value for the concentrations of each of the two tracers in the WW influences our derived meltwater fractions. In fact the concentrations themselves are unimportant, provided the gradient of the line connecting the WW properties to the much less variable CDW properties on a plot of tracer 1 versus tracer 2 (last term in parentheses in equation (3)) is unchanged. This line defines a contour of zero meltwater fraction and all other contours of equal meltwater fraction lie parallel to it (Figure 3).

In order to put a numerical value on the contours we need to evaluate the denominator in equation (4), and for this we need to know the values of the individual tracers in the meltwater. The northern ice front profiles are dominated by simple two-component mixtures of CDW and melt, which lie along an approximately straight mixing line. Since the meltwater is fresh, we can find the other tracer values simply by extrapolation of the mixing lines shown in Figure 3 to zero salinity. We obtain a temperature of -90°C and a dissolved oxygen concentration of 23 ml l^{-1} . These numbers may at first look surprising, but they have a physical explanation.

On polar ice sheets, snow that falls on the surface is transformed into firn then ice by a process of compaction. The voids within the firn are air-filled, and the inter-connectivity of these air pockets is reduced as the firn is compressed. The permeability falls to zero when the pore volume is around 130 ml kg^{-1} (Martinerie, 1992). The actual volume of air contained within the voids, measured at standard temperature and pressure (STP), will depend on the temperature and atmospheric pressure at the site of formation of the ice. Within the catchment basin of George VI Ice Shelf the ice sheet elevation is relatively low and the air temperature relatively high. The net effect might be to reduce the volume of air at STP by about 10%. Since the air is 21% oxygen, we should expect to see a dissolved oxygen concentration of around 24 to 25 ml l^{-1} in the meltwater. This is about three times the saturation level at atmospheric pressure, but at the elevated pressures found beneath the ice shelf all the gas goes into solution. Our observed concentration is not significantly different from this, given the uncertainty in the extrapolation of the O_2/S mixing line.

Salt and dissolved oxygen are conserved during the melting process such that the concentration of each in the melt is identical to that in the solid ice. However, when dealing with potential temperature it is the conservation of energy that we must consider, and in particular we must take into account the energy given up by the ocean to effect the phase change. For ice melting into CDW we can write the energy balance per unit mass as:

$$(1 - \phi)c_w(\theta_{CDW} - \theta_{mix}) = \phi c_w(\theta_{mix} - \theta_f) + \phi L + \phi c_i(\theta_f - \theta_i) \quad (5),$$

where c_w and c_i are the specific heat capacities of seawater and ice respectively, L is the latent heat of fusion of ice, and θ_i and θ_f are the temperatures of the ice shelf and freezing point respectively. The term on the left hand side is the total energy lost by the CDW, while the terms on the right hand side represent the portion of that energy loss that is used respectively for warming the meltwater from the freezing point, melting the ice and warming the ice to the freezing point. Rearranging equation (5) we can write an equation analogous to (1):

$$\theta_{mix} = (1 - \phi)\theta_{CDW} + \phi\theta_{melt} \quad (6),$$

where:

$$\theta_{melt} = \theta_f - \frac{L}{c_w} - \frac{c_i}{c_w}(\theta_f - \theta_i) \quad (7).$$

Using equation (7) we can understand our observed meltwater temperature of -90°C as the overall result of melting an ice shelf with a mean ice temperature, θ_i , of -9°C and mixing the resulting meltwater into the ocean. This relatively high ice temperature reflects the low elevation, warm catchment basin mentioned above and the fact that the far northern part of

the ice shelf is temperate (i.e. at the pressure freezing point throughout) (Paren and Cooper, 1986).

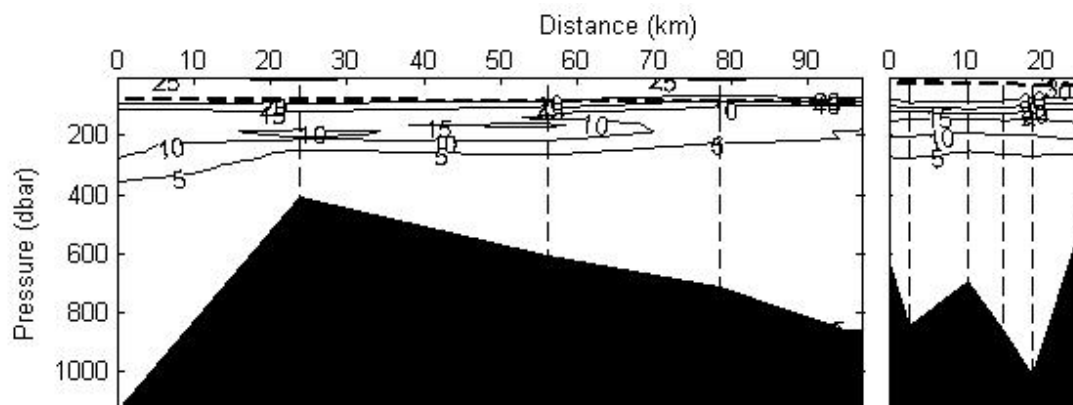


Figure 5: Sections of meltwater fraction (per mille) derived from data obtained at the southern (left) and northern (right) ice fronts. The bold dashed line indicates the depth above which atmospheric interaction disturbs the meltwater signature.

We are now in a position to calculate the meltwater concentration associated with each observation of salinity, potential temperature and dissolved oxygen, from the position of the data point in θ/S and O_2/S space (Figure 3). Clearly we must attach caveats to these calculations. There is some uncertainty in defining linear trends associated with mixing in the main pycnocline and between CDW and a meltwater source that is assumed to be uniform. Any deviations from linearity induce noise in the calculations. The assumption of approximate linearity breaks down completely in the surface mixed layer and the calculations are clearly invalid here. Equilibration with the atmosphere takes the dissolved oxygen concentration towards saturation, while other sources of freshwater reduce the salinity, without significantly altering the temperature. Fortunately these processes introduce opposite biases into the calculations of meltwater fraction; high when using θ/S data and low when using O_2/S data. We therefore use the discrepancy between the two calculations as an indication of where to disregard the results.

There are also physical bounds that we can impose on the meltwater fraction. It can be no less than zero, while equation (6) can be used to derive an upper bound, which occurs when the ocean temperature has been reduced to the freezing point ($\theta_{mix} = \theta_f$) and no further melting can occur. These limits are indicated in Figure 3. Sections of derived meltwater fraction are plotted in Figure 5. The final numbers were calculated by first bounding the two sets of values based on θ/S and O_2/S data individually to lie between the above physical limits, then taking the mean of the two. The depth above which the numbers should be disregarded is indicated in the figure. At both ice fronts the melt concentration increases above a depth of about 400 m, approximately the maximum draft of the ice shelf. The distribution across the width of the ice shelf is relatively uniform with only a slight increase to the west (left in Figure 5), where we would expect to see the strongest outflows. Concentrations are higher at the northern ice front where they reach the theoretical upper bound. We now wish to use these data in combination with velocity estimates to calculate the net meltwater transport away from the ice shelf.

Geostrophic velocities

Since we have no direct observations of currents contemporaneous with our CTD data, we must estimate them by calculating water densities and assuming that the flows are in geostrophic balance:

$$fv = g \left. \frac{\partial z}{\partial x} \right|_P \quad (8),$$

where f is the Coriolis parameter, v is velocity perpendicular to the CTD section, g is gravity, z and x are horizontal and vertical axes and the derivative is taken along isobaric surfaces. Differentiating both sides with respect to pressure and applying the hydrostatic approximation in the form:

$$\frac{\partial z}{\partial P} = -\frac{\alpha}{g} \quad (9),$$

where α is the specific volume ($1/\rho$), we arrive at:

$$f \frac{\partial v}{\partial P} = -\left. \frac{\partial \alpha}{\partial x} \right|_P \quad (10).$$

By integrating this equation with respect to pressure we can calculate the velocity on any pressure surface relative to that at a reference pressure:

$$v(P) = v(P_{ref}) + \frac{1}{f} \left. \frac{\partial}{\partial x} \left(\int_P^{P_{ref}} \alpha dp \right) \right|_P \quad (11).$$

We refer to the first term on the right-hand side of equation (11) as the reference velocity and the second term as the relative velocity. The horizontal derivative is evaluated between CTD stations and the derived velocities are then applied to the entire area between the stations. There are two problems to be overcome before we can estimate full-depth velocity profiles along our sections: defining the reference velocities, and evaluating the relative velocities below the level of the greatest common pressure on adjacent CTD stations.

The latter problem requires extrapolation of our observations into the unsampled regions. There are a number of ways of doing this and the choice is arbitrary. We adopt a strategy of extrapolating temperature and salinity in such a way that the resulting density structure gives us a predetermined simple velocity structure in the lower part of the water column. The velocity structure is derived from the vertical shear evaluated at the greatest common pressure. From this point we either keep the vertical shear constant down to the seabed, allow it to decrease linearly to zero at the seabed, or set it to zero everywhere so that the velocity stays constant from the greatest common pressure down to the seabed. We adopt the second of these as standard, but try all three options to see how sensitive our final results are to this rather arbitrary extrapolation. All other tracers are extrapolated in the same way as temperature and salinity.

To tackle the first problem, that of the reference velocity, we use our estimates of the meltwater concentration as a guide. We assume that waters with a significant meltwater content are flowing out of the cavity, while those with near zero concentrations of melt are flowing in. The divide between near zero and significant is set at a concentration of 5 per mille. Since the velocity is applied to the whole area between stations we take the mean of the meltwater concentration at adjacent stations and select the pressure at which this falls below the threshold. We set the velocity at this pressure to zero. The results are shown in Figure (6).

Constraints on the velocities

In principle we now have enough information to calculate the transport of meltwater away from the ice shelf. However, our choice of a zero velocity level is little more than an educated guess, and does not always guarantee that the upper part of the water column is flowing out of the cavity and the lower part in (Figure 6). Indeed, since there are other ice

shelves in the region, having some meltwater flowing into the cavity is perfectly reasonable. Hence there is scope to make minor adjustments to the reference velocities and in so doing ensure that the overall circulation we derive satisfies certain global constraints such as conservation of mass and tracers within the cavity. To do this we apply the well used techniques of Wunsch (1978).

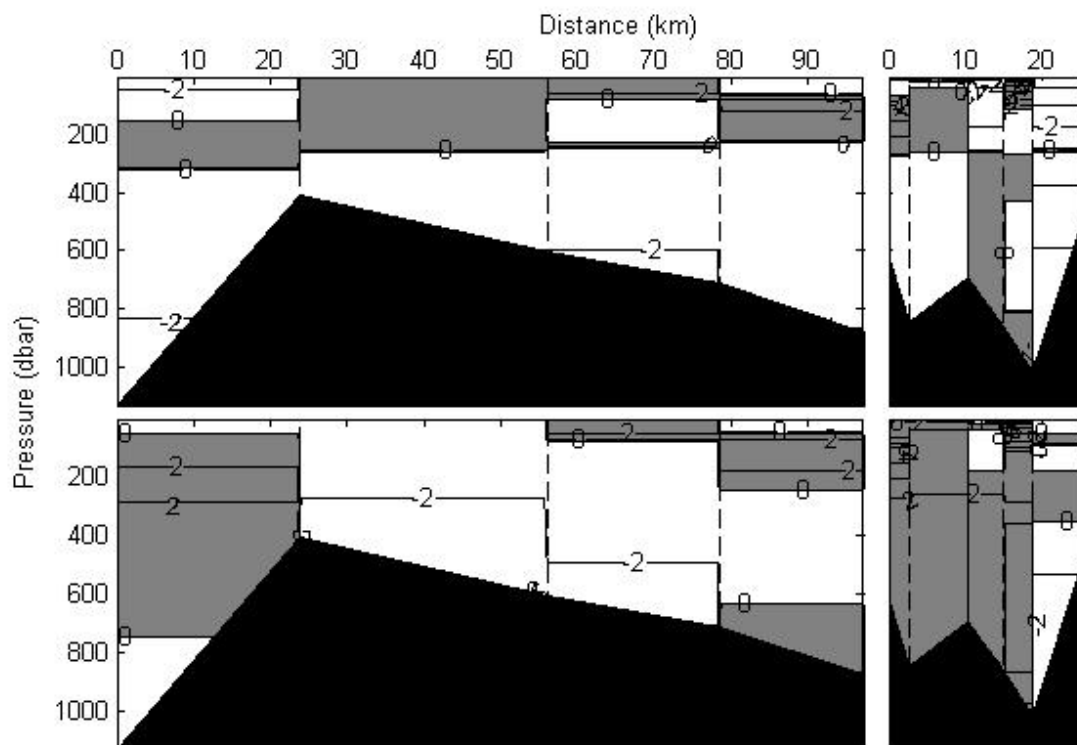


Figure 6: Initial (top) and final (bottom) velocities (cm s^{-1}) calculated at the southern (left) and northern (right) ice fronts. Positive values (shaded) indicate flow out of the cavity (into the page). The initial velocities were set to have a level of zero motion along the 5 per mille meltwater fraction contour (Figure 5). The final velocities represent a minimal adjustment to the initial values that will permit overall balanced budgets for the tracers.

Since our CTD sections effectively close off the cavity, we know that the total mass transport across them must fit with the constraint:

$$\sum_{j=1}^n (M_{out} - M_{in})_j = M_{melt} \quad (12),$$

where M is mass and the summation runs over n individual station pairs. Similarly total transport of tracers must satisfy:

$$\sum_{j=1}^n [(M\chi)_{out} - (M\chi)_{in}]_j = M_{melt} \chi_{melt} \quad (13).$$

Combining these we can eliminate the unknown melt rate:

$$\sum_{j=1}^n \{ [M(\chi - \chi_{melt})]_{out} - [M(\chi - \chi_{melt})]_{in} \}_j = 0 \quad (14),$$

and the transport between each station pair can be obtained from an integration of the velocity profile with respect to pressure:

$$[M(\chi - \chi_{melt})]_{out} - [M(\chi - \chi_{melt})]_{in} = \frac{1}{g} \int_{P_{bot}}^{P_{top}} v(p) [\chi(p) - \chi_{melt}] \Delta x(p) dp \quad (15),$$

where Δx is the width of the gate; constant with pressure except in the unsampled region where we assume it decreases linearly to zero (i.e. the areas between adjacent stations are made trapezoidal in shape through the addition of a bottom triangle).

The velocity in equation (15) comprises two parts, the known relative velocity, v_{rel} , which we obtained from the measured specific volume profiles, and the unknown reference velocity, v_{ref} . Equation (14) thus contains n unknown reference velocities, and we have m such equations, one for each observed tracer, that can be written in matrix form as:

$$\mathbf{A}\mathbf{v} + \mathbf{b} = \mathbf{0} \quad (16),$$

where:

$$A_{ij} = \frac{1}{g} \left\{ \int_{P_{bot}}^{P_{top}} [\chi_i(p) - \chi_{melt}] \Delta x(p) dp \right\}_j \quad (17),$$

$$b_i = \frac{1}{g} \sum_{j=1}^n \left\{ \int_{P_{bot}}^{P_{top}} v_{rel}(p) [\chi_i(p) - \chi_{melt}] \Delta x(p) dp \right\}_j \quad (18),$$

and:

$$v_j = (v_{ref})_j \quad (19).$$

In practice we have fewer equations than unknowns ($m < n$), so equation (16) has no unique solution. The procedure described by Wunsch (1978) allows us to choose from the infinite number of possible solutions the one that has the smallest vector, \mathbf{v} . Since our initial educated guess at the circulation set the reference velocities to zero, this particular solution represents the smallest possible adjustment to our initial guess that will allow us to satisfy the constraints imposed by equation (14). In formulating equation (16) we use the three tracers, potential temperature, salinity and dissolved oxygen, for which we have full-depth continuous profiles. The integrals in equations (17) and (18) are performed over the entire depth of the water column.

Results

The resulting velocity sections are shown in Figure 6. We find that the tracer budgets (equation (14)) can be satisfied with relatively small velocities, less than 2 cm s^{-1} in magnitude, applied at the reference levels. The solutions appear physically reasonable in that the strongest outflows appear against the western coast, while the inflows are generally in the east. The overall structure found for the northern ice front section shows many of the features found by Potter et al. (1988), although the weak inflow that they postulated to occur everywhere below about 400 m is absent. In fact there is a net outflow of 0.23 Sv across our northern section that is balanced by a net inflow across the southern section. Such a net throughflow from south to north is consistent with our earlier finding that the northern ice front is dominated by CDW sourced from the south.

Now combining the results in Figure 6 with those in Figure 5 we can calculate the transport of meltwater in and out of the cavity. When using the meltwater concentration in this way, we exclude the upper part of the water column where the values are unreliable. At the southern ice front the derived meltwater outflow of $61 \text{ km}^3 \text{ yr}^{-1}$ is almost offset by an inflow of $57 \text{ km}^3 \text{ yr}^{-1}$. At the northern ice front only $7 \text{ km}^3 \text{ yr}^{-1}$ flow into the cavity while $79 \text{ km}^3 \text{ yr}^{-1}$ flow out. The net production of meltwater within the cavity then totals $76 \text{ km}^3 \text{ yr}^{-1}$. This last figure can also be estimated from the net flow out of the cavity (equation (12)), which in this case is 0.002 Sv or $72 \text{ km}^3 \text{ yr}^{-1}$. Drawn from the $25,000 \text{ km}^2$ area of the ice shelf, these numbers suggest a mean melt rate close to 3 m yr^{-1} .

These numbers are fairly insensitive to the procedure we use to extrapolate data into the unsampled parts of the section. The ranges we derive using all three methods described above are $67\text{-}77 \text{ km}^3 \text{ yr}^{-1}$ for the net melt rate and $0.21\text{-}0.23 \text{ Sv}$ for the south to north

throughflow. Similarly the results are not greatly altered if we choose a different reference level where the velocity is initially set to zero, e.g. the sea surface, the seabed, a selected isotherm, etc. Trying a number of different options gave us ranges of 63-77 km³ yr⁻¹ and 0.15-0.26 Sv, respectively. Formal error estimates are quite difficult, because most of the uncertainty arises from the assumptions we made in calculating the velocity profiles: that the flow is geostrophic and steady.

Potter and Paren (1985) estimated an equilibrium melt rate of 2.1 m/yr for the ice shelf as a whole, while time-series data at ERS altimeter cross-over points indicates that the ice shelf is thinning at a rate of 1 m yr⁻¹ (A. Shepherd, personal communication). Together these suggest an average net melt rate of around 3 m/yr. Coincidentally Corr et al. (2002) measured a melt rate of 2.8 m/yr over a twelve-day period in December 2000 at one point near the southern end of the ice shelf.

Perhaps the most unsatisfactory aspect of the results is the low net meltwater flux across the southern ice front. If we assume that the ridge of maximum ice thickness acts as a melt watershed, then 2/5 of the basal area supplies melt to the southern outflows and 3/5 to the northern outflows. There is no reason to expect dramatically lower melt rates in the south. Potter and Paren (1985) estimated similar equilibrium melt rates for north and south, and the measurement of Corr et al. (2002) was made near the region of maximum ice thickness. The apparently poorer results for the southern ice front may be because some of the melt signature is lost by upwelling and mixing into the surface layers (Figure 5). At the northern ice front, at the time of the observations, the meltwater was upwelling beneath a fast ice cover which protected it from the atmosphere and preserved the meltwater signature until the water was sampled directly at the fast ice edge. Of course the southern ice front section also suffers from poorer horizontal resolution, so some of the details of the outflows could have been missed.

Summary and conclusions

We have discussed the results of near synchronous surveys of the oceanographic conditions at the northern and southern ice fronts of George VI Ice Shelf. The observations included measurements of potential temperature, salinity and dissolved oxygen concentrations, all of which provide information on the fraction of meltwater derived from the ice shelf base present in the water column. Melt appears at both ice fronts above the level of the maximum ice shelf draft. We find higher meltwater concentrations at the northern ice front, up to the theoretical maximum, but the signature of any similarly concentrated outflows could have been lost at the southern ice front by upwelling close to the ice shelf.

From the observed density profiles we derived relative geostrophic velocities across the sections. We then estimated absolute velocities by applying constraints on the overall transports of potential temperature, salinity and dissolved oxygen, following the procedures of Wunsch (1978). This enabled us to quantify the transport of meltwater away from the cavity and the overall transport of water through the cavity. We estimate a mean melt rate of around 3 m yr⁻¹ for the ice shelf and a net flow from south to north of around 0.2 Sv. These numbers are consistent with earlier observations of melting and thinning of the ice shelf and with our observation that the CDW we found at the northern ice front came from Ronne Entrance rather than Marguerite Bay.

Acknowledgements

We are grateful to the officers and crew of *Nathaniel B. Palmer* and all participants in cruise NBP9402 for their assistance in the collection of the data presented here. Subsequent collaborative work on the data has been supported by NSF award ANT 02-33303.

References

- Bentley, M.J., D.A. Hodgson, D.E. Sugden, S.J. Roberts, J.A. Smith, M.J. Leng and C. Bryant. 2005. Early Holocene retreat of the George VI Ice Shelf, Antarctic Peninsula, *Geology*, **33**(3): 173–176.
- Bishop, J.F. and J.L.W. Walton. 1981. Bottom melting under George VI Ice Shelf, Antarctica, *J. Glaciol.*, **27**(97): 429–447.
- Corr, H.F.J., A. Jenkins, K.W. Nicholls and C.S.M. Doake. 2002. Precise measurement of changes in ice-shelf thickness by phase-sensitive radar to determine basal melt rates, *Geophys. Res. Lett.*, **29**(8), 1232.
- Doake, C.S.M. and D.G. Vaughan. 1991. Rapid disintegration of the Wordie Ice Shelf in response to atmospheric warming, *Nature*, **350**(6316): 328–330.
- Giulivi, C.F. and S.S. Jacobs. 1997. Oceanographic Data in the Amundsen and Bellingshausen Seas, N.B. Palmer Cruise 9402, Feb-Mar 1994, *TR LDEO-97-3*, Palisades NY, 330pp.
- Hellmer, H.H., S.S. Jacobs and A. Jenkins. 1998. Oceanic erosion of a floating Antarctic glacier in the Amundsen Sea, in *Ocean, Ice, and Atmosphere: Interactions at the Antarctic Continental Margin*, edited by S.S. Jacobs and R.F. Weiss, *Antarct. Res. Ser.*, **75**: 83–99.
- Jenkins, A. 1999. The impact of melting ice on ocean waters, *J. Phys. Oceanogr.*, **29**(9): 2370–2381.
- Lennon, P.W., J. Loynes, J.G. Paren and J.R. Potter. 1982. Oceanographic observations from George VI Ice Shelf, Antarctic Peninsula, *Ann. Glaciol.*, **3**: 178–183.
- Lucchitta, B.K. and C.E. Rosanova. 1998. Retreat of northern margins of George VI and Wilkins ice shelves, Antarctic Peninsula, *Ann. Glaciol.*, **27**: 41–46.
- Martinerie, P., D. Raynaud, D.M. Etheridge, J.-M. Barnola and D. Mazaudier. 1992. Physical and climatic parameters which influence the air content in polar ice, *Earth and Planet. Sci. Lett.*, **112**(1–4): 1–13.
- O’Cofaigh, C., J.A. Dowdeswell, C.S. Allen, J.F. Hiemstra, C.J. Pudsey, J. Evans and D.J.A. Evans. 2005. Flow dynamics and till genesis associated with a marine-based Antarctic palaeo-ice stream, *Quat. Sci. Rev.*, **24**(5–6): 709–740.
- Paren, J.G. and S. Cooper. 1986. George VI Ice Shelf: a temperate ice shelf, *Filchner-Ronne Ice Shelf Programme, Report No. 3*: 62–63.
- Potter, J.R. and J.G. Paren. 1985. Interaction between ice shelf and ocean in George VI Sound, Antarctica, in *Oceanology of the Antarctic Continental Shelf*, edited by S.S. Jacobs, *Antarct. Res. Ser.*, **43**: 35–58.
- Potter, J.R., J.G. Paren and J. Loynes. 1984. Glaciological and oceanographic calculations of the mass balance and oxygen isotope ratio of a melting ice shelf, *J. Glaciol.*, **30**(105): 161–170.
- Potter, J.R., M.H. Talbot and J.G. Paren. 1988. Oceanic regimes at the ice fronts of George VI Sound, Antarctic Peninsula, *Contin. Shelf Res.*, **8**(4): 347–362.
- Sugden, D.E. and C.M. Clapperton. 1981. An ice-shelf moraine, George VI Sound, Antarctica, *Ann. Glaciol.*, **2**: 135–141.
- Wunsch, C. 1978. The North Atlantic general circulation west of 50°W determined by inverse methods, *Rev. Geophys. Space Phys.*, **16**(4): 583–620.